Multistatic specular meteor radar network in Peru: System description and initial results

J. L. Chau[1]*, J. M. Urco[1], J. Vierinen[2], B. J. Harding[3], M. Clahsen[1], N. Pfeffer[1], K. M. Kuyeng[4], M. A. Milla[4], P. J. Erickson[5]

[1]Leibniz Institute of Atmospheric Physics at the University of Rostock, Kühlungsborn, Germany
[2]Arctic University of Norway, Tromso, Norway
[3]Space Sciences Laboratory, University of California, Berkeley, CA, USA
[4]Radio Observatorio de Jicamarca, Instituto Geosfísico del Perú, Lima, Peru
[5]MIT Haystack Observatory, Westford, MA, USA

Key Points:

- Measurements of horizontal wind gradients at low latitude mesosphere and lower thermosphere altitudes.
- These gradients of the horizontal winds show strong temporal and altitude variability that are not observed at high latitudes.
- Improved vertical wind measurements are obtained using a gradient wind-field analysis method inherently free from horizontal divergence contamination.

*Schloss Str. 6, Kuehlungsborn, 18225, Germany

Corresponding author: J. L. Chau, `chau@iap-kborn.de`

Abstract

The mesosphere and lower thermosphere (MLT) region is dominated globally by dynamics at various scales: planetary waves, tides, gravity waves, and stratified turbulence. The latter two can co-exist and be significant at horizontal scales less than 500 km, scales that are difficult to measure. This study presents a recently deployed multi-static specular meteor radar system, SIMONe Peru, which can be used to observe these scales. The radars are positioned at and around the Jicamarca Radio Observatory, which is located at the magnetic equator. Besides presenting preliminary results of typically reported large scale features, like the dominant diurnal tide at low latitudes, we show results on selected days of spatially and temporally resolved winds obtained with two methods based on: (a) estimation of mean wind and their gradients (gradient method), and (b) an inverse theory with Tikhonov regularization (regularized wind field inversion method). The gradient method allows improved MLT vertical velocities and, for the first time, low-latitude wind field parameters such as horizontal divergence and relative vorticity. The regularized wind field inversion method allows the estimation of spatial structure within the observed area and has the potential to outperform the gradient method, in particular when more detections are available or when fine adaptive tuning of the regularization factor is done. SIMONe Peru adds important information at low latitudes to currently scarce MLT continuous observing capabilities. Results contribute to studies of the MLT dynamics at different scales inherently connected to lower atmospheric forcing and E-region dynamo related ionospheric variability.

Plain Language Summary

The mesosphere and lower thermosphere (MLT) region is dominated by neutral wind dynamics with structure scales ranging from a few thousands of kilometers down to a few kilometers. In this work, we present a new state-of-the-art ground-based radar system using multistatic meteor scattering that allows tomographic studies of MLT wind dynamics at scales not possible before. Given the location of the radar network at the magnetic equator, its focus is on wind dynamics peculiar to equatorial latitudes. Two methods for estimating the mesospheric neutral wind field are used. One takes into account wind gradients in addition to mean wind (gradient method). The other estimates a spatially resolved wind vector field and uses an additional mathematical constraint that produces smooth wind field solutions (regularized wind field inversion method). Using the gradient method, the vertical wind estimate is improved. For the first time at MLT equatorial latitudes, parameters familiar to meteorologists, such as horizontal divergence and relative vorticity are obtained. Measurements from this new system have the potential to contribute to coupling studies of the atmosphere and the ionosphere at low latitudes.

1 Introduction

The mesosphere and lower thermosphere (MLT) region between 60 and 110 km forms the boundary between the lower atmosphere and space. This region is dominated by atmospheric dynamics including planetary waves, tides, gravity waves, and stratified turbulence. The main sources of these dynamics lie mainly in the lower atmosphere. Similarly, neutral dynamics and electrodynamics at higher altitudes can be modified by locally generated MLT dynamics or by perturbations propagating from below and interacting with the MLT region (e.g., Vincent, 2015, and references therein).

MLT large scale dynamics, either from wind or temperature measurements, have been extensively studied in the last two decades with ground- and satellite-based instruments and with general circulation models (GCMs). There has been significant progress in the understanding of these dynamics particularly in their mean flows, planetary waves, and tidal parameters (Pancheva & Mukhtarov, 2011; Vincent, 2015). For example, it is

67 well known that semidiurnal tides dominate at mid and high latitudes, while at low lat-
68 itudes, diurnal tides are more important (e.g., Smith, 2012).

69   In addition to dominant MLT diurnal tides at low latitudes (e.g., Davis et al., 2013),
70 other salient MLT large scale dynamics peculiar to low latitudes occur: ultra fast Kelvin
71 waves (UFKW) with periods of 3 to 4 days, quasi-two-day waves (QTDW), the meso-
72 spheric semiannual oscillation (MSAO), and the mesospheric quasi-biennial enhancement
73 (MQBE) (Abdu et al., 2015; Pancheva & Mukhtarov, 2011; Venkateswara Rao, Tsuda,
74 Riggin, et al., 2012). Previous observational contributions to these studies from single
75 ground-based stations have been focused on providing excellent time coverage, but they
76 have lacked spatial (wave number) information. Therefore, single-station ground-based
77 observations at low latitudes have usually been complemented with GCMs to complete
78 the spatiotemporal picture (e.g., Davis et al., 2013).

79   MLT dynamics at low latitudes has been shown to have important influence on iono-
80 spheric and thermospheric variability at different scales. For example, large ionospheric
81 perturbations have been associated with sudden stratospheric warming (SSW) events,
82 which are initiated in the winter polar stratosphere but produce global changes (e.g., Pe-
83 datella et al., 2018). Additionally, enhanced ionospheric perturbations associated with
84 lunar tide enhancement have been observed and modeled at low latitudes (e.g., Chau et
85 al., 2009; Goncharenko et al., 2010; Fejer et al., 2010; Pedatella et al., 2012; Chau et al.,
86 2012). Similarly, modulations of F-region electron densities around the magnetic equa-
87 tor have been attributed to effects of non-migrating diurnal tides (Immel et al., 2006;
88 England, 2012). Both of these atmospheric and ionospheric coupling examples at low lat-
89 itudes are in turn attributed to an imprinting of MLT dynamics through the so-called
90 E-region dynamo. Recently, the NASA Ionospheric Connection Explorer (ICON) mis-
91 sion has started operation to study these and other atmospheric and ionospheric cou-
92 pling processes at low latitudes (e.g., Immel et al., 2018).

93   Monostatic specular meteor radars (SMRs) have been widely used to study MLT
94 dynamics. These radars are able to measure MLT dynamics from 75 to 105 km contin-
95 uously by providing horizontal winds averaged on areas of ~400 km diameter at 1–2 hour
96 cadence with 2–4 kilometer altitude resolution. In the case of mid and high latitudes,
97 SMRs from different longitudes at selected mid and high latitude bands have been an-
98 alyzed together to provide spatial (wavenumber) information on dominant tides and plan-
99 etary waves (e.g., Manson et al., 2009; He et al., 2018).

100   In this work we present the first results from a multistatic SMR installed at and
101 around the Jicamarca Radio Observatory in Peru. This system joins a small list of SMRs
102 located at low latitudes, here defined as between $\pm15°$ latitude (see Venkateswara Rao,
103 Tsuda, Riggin, et al., 2012; Davis et al., 2013; Araújo et al., 2014; Rao et al., 2014, for
104 references and results of other low latitude SMRs). All of these previous systems have
105 operated in a monostatic mode, where transmitter and receivers are co-located. Multi-
106 static SMR capabilities from this new system in Peru add considerably to these obser-
107 vational capabilities through studies of large scale dynamics in combination with other
108 low latitude ground-based radars. In particular, the combination is able to separate space-
109 time observational ambiguities, similar to other studies conducted at mid and high lat-
110 itudes (Murphy et al., 2006; Manson et al., 2009; He & Chau, 2019).

111   A multistatic SMR brings the possibility of more scattering detections and point-
112 ing diversity through provision of different viewing angles. The former helps to provide
113 standard measurements with better quality, while the latter allows spatial measurements
114 of MLT winds within the illuminated area (Stober & Chau, 2015; Chau et al., 2017). Mul-
115 tistatic capabilities provide attractive, and straightforward, observational products, in
116 particular estimation of the horizontal wind gradients, in a manner similar to previous
117 successful studies of the lower atmosphere and thermosphere (e.g., Browning & Wexler,
118 1968; Burnside et al., 1981). These horizontal gradients are important for proper esti-

mation of several key MLT parameters. For example, using two links (from two closely-located monostatic SMRs), Chau et al. (2017) found that the vertical wind estimate is contaminated by horizontal divergence if horizontal gradients of the horizontal wind are not considered. In addition, they reported the climatology of horizontal divergence and relative vorticity in the Arctic MLT region. Using these horizontal divergence estimates, Laskar et al. (2017) provided reasonable estimates of mean summer mesospheric vertical winds, using the mass continuity equation and assuming an anelastic flow, i.e., incompressible and stratified.

The multistatic SMR results reported here originated in a concept called MMARIA (Multi-static, Multi-frequency Agile Investigations of the Atmosphere) (Stober & Chau, 2015) whose primary goal was to add interferometric receivers located with 60–200 km radius from existing transmitters. In this work we have implemented MMARIA through a project named SIMONe. SIMONe (Spread Spectrum Interferometric Multistatic meteor radar Observing Network) makes use of coded continuous waves, multiple-input multiple-output (MIMO), and compressed sensing concepts (Vierinen et al., 2016; Urco et al., 2018, 2019). Compared to the original system architecture, SIMONe allows MMARIA implementations to be cheaper and more robust, with easier implementation of additional bistatic links, as only a single receiver antenna is needed for each bi-static receiver station (e.g., Chau et al., 2019).

Beyond implementation specifics and inherent horizontal resolution capability of MLT winds (e.g., Chau et al., 2017; Stober et al., 2018), multistatic SMRs can be also used to improve the estimation of kinetic energy and momentum fluxes at regional scales. In particular, analysis can either estimate average values of these quantities in a manner similar to traditional techniques used in monostatic SMRs (e.g., Hocking, 2005), or further analysis can produce important information on spatio-temporal features using second-order statistics between detections (e.g., Vierinen et al., 2019). The former requires subtraction of large scale wind contributions (means and tides) to yield values which represent GW contributions (e.g., Andrioli et al., 2013). This approach has been implemented previously in a bistatic configuration in Australia by Spargo et al. (2019), and obtained an increase of precision on momentum flux estimates mainly due to an increased number of detections. The latter method of employing second-order statistics between detections has been implemented with 24 hours of data in a special campaign that consisted of fourteen bistatic links in northern Germany. Although momentum fluxes were not reported given the relatively short duration of collected data, spatial (3D) and temporal correlation, structure and spectral functions were obtained as detailed in Vierinen et al. (2019).

As in the case of mid and high latitudes, measurement of GW momentum fluxes represents one of the most challenging and needed tasks at low latitudes (e.g., Fritts & Alexander, 2003). Not only is this information needed to improve GCMs, but observations are furthermore key to understanding different MLT processes. For example, Venkateswara Rao, Tsuda, and Kawatani (2012) reported significant correlations between the strength of MSAO and short-period GW variances at mesospheric altitudes over Indonesia, suggesting that GW momentum deposition drives the MSAO. However, GW momentum flux measurements are still needed to validate this hypothesis.

Our system, SIMONe Peru, represents one of the first two operational multistatic SMRs with MIMO and spread-spectrum technology. The second system has been installed in southern Argentina (SIMONe Argentina). Both system have been running continuously since October 2019. In this work, besides the system description, we present preliminary multistatic SMR results with emphasis on neutral winds.

This study begins by describing in detail a general SIMONe system, followed by the specifics of the SIMONe Peru installation. Three methods for obtaining wind fields are then presented: (1) homogeneous method; (2) gradient method; and (3) a regular-

171 ized wind field inversion method. MLT wind results for large-scale features are presented
172 for the first six months of data, while mesoscale features are shown for selected times in
173 section 4. Using the spatial information provided by the multistatic method, our anal-
174 ysis places special emphasis on quantifying contamination of vertical wind components
175 by horizontal wind divergence if horizontal gradients are not considered. Observations
176 of other atmospheric and ionospheric targets are presented and discussed in section 5.
177 Finally, a summary of main results and future plans is presented.

2 System description

179 The SIMONe concept was introduced and described by Chau et al. (2019) and later
180 used on a special seven-day campaign in northern Germany (e.g., Vierinen et al., 2019).
181 In both cases, the concept was implemented using hardware and software prototypes.
182 In this section, we describe in detail our most recent SIMONe implementation in gen-
183 eral and the specifics of SIMONe Peru. A general architectural description is useful since
184 a similar system has also been installed in Argentina (SIMONe Argentina), and two new
185 systems will be installed in northern Germany and northern Norway in the near future.

2.1 A general description of SIMONe

187 SIMONe uses modern radar approaches, such as spread spectrum, MIMO, and com-
188 pressed sensing, to study the MLT region with a multistatic radar configuration. On trans-
189 mission, multiple antennas (e.g. multiple input) are used in an interferometer configu-
190 ration of at least five antennas, each of them fed by an independent transmitter. Each
191 transmitter uses coded continuous wave (CW) waveforms with a different pseudo-random
192 binary code on each transmitter (e.g., Vierinen et al., 2016). To limit inter-station in-
193 terference, the seeds of the random number generators producing the codes are carefully
194 selected to minimize cross-correlations among all codes

195 On reception, a SIMONe station can consist of one antenna or more antennas ar-
196 ranged in an interferometer configuration. The former allows the implementation of MISO
197 link (i.e., Multiple-Input, Single Output). On the other hand, multiple receive antennas
198 allow either a SIMO (Single-Input Multiple Output; one coherent transmit signal) or a
199 MIMO (Multiple-Input Multiple-Output; multiple coherent transmit signals) link. SIMO
200 is the standard configuration of monostatic SMRs, where the angle-of-arrival (AOA) is
201 measured, defined as incoming ray angle with respect to the receiver array. In the case
202 of a MISO configuration, the angle-of-departure (AOD) is measured as the ray angle with
203 respect to the transmitter, while in MIMO configurations, AOAs and AODs are mea-
204 sured simultaneously from the same target (e.g., Chau et al., 2019, for more details).

205 Figure 1 shows a block diagram of the main components of a typical SIMONe sys-
206 tem, arranged as transmitter, receiver, and radar signal processing (RSP). On transmis-
207 sion, we use 450-W continuous wave (CW) power amplifiers (HPA) manufactured by Hilber-
208 ling on each antenna. The digital transmitter unit (DTX) creates HPA driver signals as
209 a low-power phase-modulated CW signal that is generated by a software defined radio
210 unit, currently implemented as a National Instruments USRP N200 with a BasicTX trans-
211 mitter daughter board. DTX units are commanded with modulating signal information
212 by a radar signal generator (RSG) inside the transmitter computer. The RGS receives
213 user instructions related to waveform, code, baud rate, period, amplitude, and phase.
214 The main computer is connected to the internet for remote control functionality, and to
215 an uninterrupted power supply (UPS). A Trimble global position system (GPS) receiver
216 unit provides a globally coherent 10 MHz reference clock and one pulse-per-second (PPS)
217 signal to the DTX for multi-static synchronization, and provides timing information to
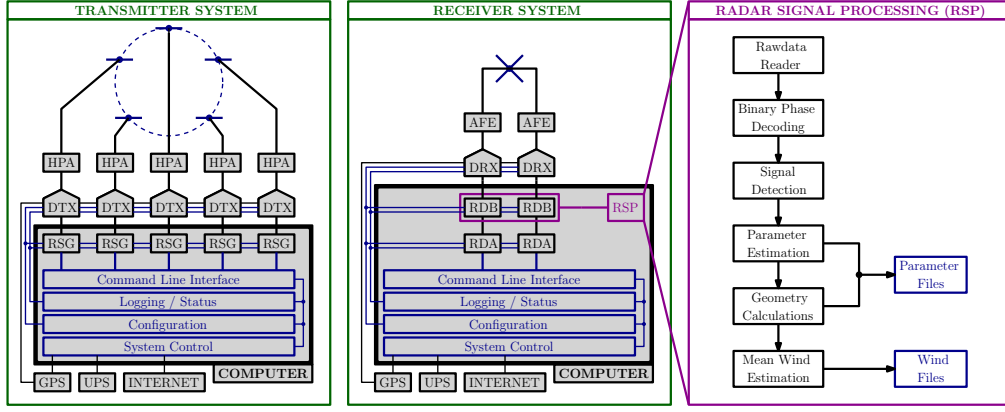218 the computer.

Figure 1. SIMONe system block diagram: (left) transmitter, (middle) receiver, and (right) radar signal processing (RSP).

On reception, signals from each antenna are amplified and filtered by an analog front end (AFE). The amplified signals are fed into a Digital Receiver (DRX), implemented as a National Instruments USRP-N200 with a BasicRX receiver daughter board. Signals from two antennas are fed to each DRX. Inside the DRX, the signal is digitized, down-converted to in-phase and quadrature components, and decimated. The digital samples are stored by the receiving computer in a raw data buffer (RDB) and a raw data archive (RDA). Data storage employs MIT Haystack Observatory's Digital RF coherent RF data package (`https://github.com/MITHaystack/digital_rf`), in which each complex RF voltage level sample is coherently referenced to the Unix time standard (fractional seconds since 0000 UTC 1970-01-01) and recorded in Hierarchical Data Format version 5 (HDF5) with tagged metadata. The RDB stores up to one hour of data in ring-buffer configuration and is used for real-time processing and monitoring. The RDA stores up to 14 days of data in ring-buffer configuration and this deeper buffer is used for off-line routine analysis or externally triggered processing of special events (e.g., bolides). The receiving computer is connected to the internet for remote control and data transfer. As in the case of the transmitter, a Trimble GPS receiver unit provides a globally coherent 10 MHz reference clock and 1 PPS to the USRP-N200, and timing information to the computer. The precision of the 1 PPS edge is less than 25 ns, while the frequency jitter of the reference clock is a fraction of 1 Hz, providing SIMONe with excellent range synchronization and Doppler capability.

The receiver and transmitter computers run a Linux operating system (Ubuntu distribution). Internet connection depends on system location, but is flexible. For example, we have used a combination of wired internet service provider with either dynamic or static IP address, as well as wireless internet using an available cellular phone company.

The radar signal processing (RSP) modules have been developed in the Python computing language and are run on the receiving computer. Incoming digital complex samples are decoded using the compressed sensing approach developed by Urco et al. (2019). Specifically, signals are decoded using a sparse model with a combination of matched filter, inverse filter, and least square fitting, and yield the signal from each transmitter on each receiver. Combinatorics indicate that in the case of a typical MISO configuration (five transmitters and one receiver with two polarizations) ten complex signals are obtained. Fifty complex signals are obtained in the case of a MIMO configuration consisting of five transmitters and five receivers with two polarizations each. The decoded sig-

nals are incoherently combined to detect echoes, and the decoded signals are stored. The received complex signals of the two linear polarizations are coherently combined taking into account their polarization angle. This operation allows us to use all the available power on reception, since the received signals are in general elliptically polarized depending on the bistatic geometry, the orientation, and location of the echoes. After coherent combination, auto and cross correlations are estimated to determine Doppler shift, correlation time, amplitudes, and interferometric phases using fitting approaches (parameter estimation). Depending on the goodness of fit and the characteristics of the detected echoes, events are selected and identified for further processing. The parameters of identified events and geometry calculations, assuming the system is phase calibrated, for each link are recorded on site and sent via internet to a central server. Separate system phase calibration is performed. Geometry calculations take into account the Earth's curvature and produce estimates of the latitude, longitude, altitude, and Bragg wave vector (see below) for each identified event. On-site, mean winds are estimated, visualized and stored for monitoring and quality control purposes.

2.2 Peru deployment

The SIMONe Peru system is a specific implemention of the SIMONe concept, and currently consists of one transmitter site located at the Jicamarca Radio Observatory (JRO) (11.95°S, 76.87°W, 540.55 m) and five receiver stations located between 30 and 180 km from JRO. The operating frequency is 32.55 MHz. The transmitter site is composed of five linearly-polarized two-element Yagi antennas, with the elements aligned in the East-West direction, located at positions (x, y, z): (11.71, -15.8, 0), (18.428, 6.345, 0.436), (-0.48, 19.58, 0.15), (-18.64, 5.66, -0.67), (-11.2, -16.067, -0.732), respectively, in meters with respect to the center of the array. Note that the interferometry configuration is a pentagon and all the antennas are not on plane, i.e., z is not zero for all the antennas. The use of a pentagon configuration in interferometric SMRs has been discussed by Younger and Reid (2017) and Chau and Clahsen (2019). Point-spread functions of pentagon configured multistatic SMRs show sidelobes with lower amplitude, more angular separation and better symmetry than those obtained with the Jones configuration that is used in most monostatic SMRs (e.g., Jones et al., 1998).

Each receiver site consists of one cross-polarized two-element Yagi antenna, where each linear polarization is received independently. A list of the receiver sites, their location and time of operations between September 2019 and April 2020 is given in Table 1. Although our current system consist of only five receiver units, during this time period we have located them at more sites due to: (a) logistical issues (e.g., unexpected electromagnetic interference), and (b) exploration of potential sites for future campaigns with more receiving stations.

Since the transmitter site uses multiple transmitters (five) and each receiver site uses only one receiver antenna, the current version of SIMONe Peru therefore operates in a MISO configuration. Each transmitter uses a different pseudo-random code of 1000 bauds with baud length of 10 μs, so the waveform sequence is repeated at 10 ms intervals, providing an unambiguous total range of 3000 km.

An example of typical detections over the JRO-Azpitia bistatic link is shown in the supplemental material (Figure S1). Besides the specular meteor echoes, which are the main focus of SIMONe Peru, other echoes are also noted with strong radar cross sections. In Figure S1, the strong echoes slightly above 200 km around 1800 UT are due to daytime equatorial electrojet field-aligned irregularities (e.g., Farley, 2009). Examples of other echoes are presented and discussed in section 5.

The parameter files of each station are quality-controlled by processing at our home institute in Germany. Since the cross-correlations of all interferometric pairs are recorded for each identified event, the empirical phase calibration algorithm of Chau and Clah-
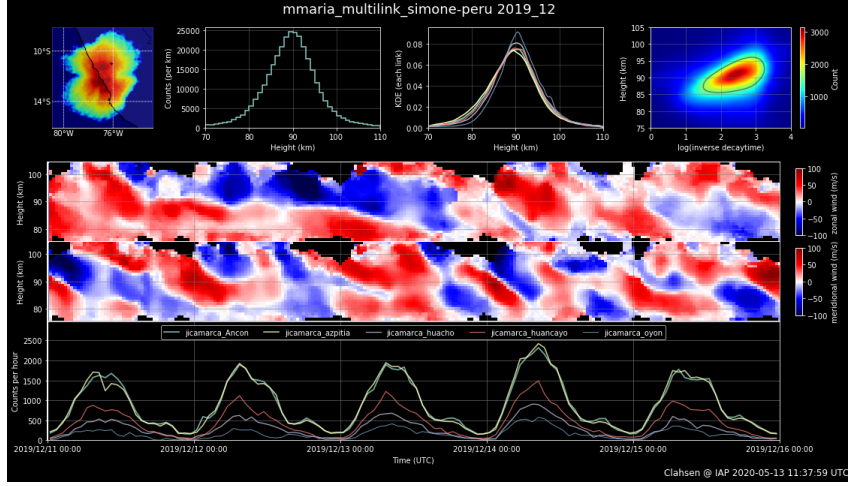
Figure 2. Example of parameters obtained after combining five SIMONe Peru links: (a) 2D histogram of detections on latitude vs longitude axes, (b) altitude distributions across all links, (c) altitude distribution of each link, (d) 2D histogram altitude vs inverse decay time, (e) mean zonal winds, (f) mean meridional winds, and (g) counts per hour for each bistatic link.

sen (2019) is applied where needed and a new parameter file with recalculated geometry is generated. In practice, we have only found it necessary to use empirical phase calibration during initial installation and checkout activities. Since then, the system are hardware calibrated and exhibit long term stability using periodic manual checks. Motivated by the detection of strong daytime EEJ echoes and concerns about their effect on core MLT processing, we implemented additional quality control measures through use of the clustering algorithm DBSCAN (Ester et al., 1996) to find clusters of echoes along individual range, time and angle axes and remove them. The process is robust to the SMR application because specular meteor echoes are not expected to be clustered in all three variables. After the DBSCAN based quality control process, the files of all links are combined into a meta-structure known as a multilink file. Figure 2 shows an example of a few days of observations in December 2019 after combining the five links. These files are stored in our database and used in the results presented below.

In Figure 3 we show a map with all SIMONe Peru stations between October 2019 and April 2020, where blue represents the transmitter station. The receiving stations are represented by: green (currently running), yellow (waiting to resume operations), red (tested but currently not in operation). The right panel shows a summary of operations during the first six months: (top) normalized counts color coded by links, and (bottom) average total daily count for each month. The links with the most meteor detections are JRO-Azpitia and JRO-Ancon. Seasonally, December is the month with most events (more than 40,000 per day). Note that in January, the JRO-Ancon link shows significantly fewer counts than December and February due to a site problem with electricity and internet during that month.

3 Wind processing

The phase of the received complex voltage at receiving antenna m due to a meteor echo located in the far field and illuminated by transmitter p, i.e., phase of V_{mp}, is:

$$\phi_{mp} = -(\mathbf{k}_i - \mathbf{k}_s) \cdot \mathbf{u}t - \mathbf{k}_i \cdot \mathbf{R}_p - \mathbf{k}_s \cdot \mathbf{R}_m \tag{1}$$
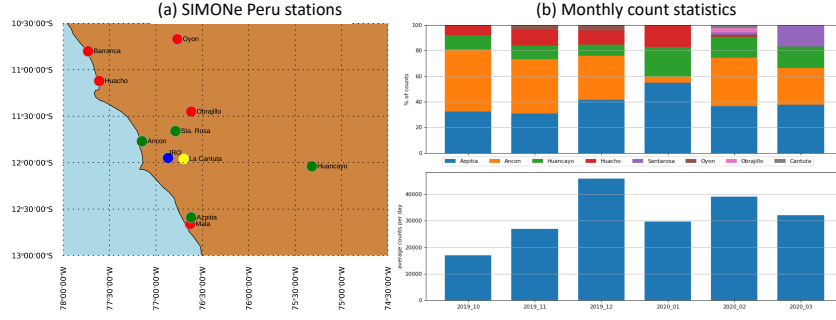
Figure 3. (a) Map showing SIMONe Peru stations: transmitter in blue and receiving stations in green, yellow and green representing running, waiting to resume operations, and tested but not running, respectively. (b) Count statistics between October 2019 and March 2020 for each month. The top graph shows the detections in percentage color coded for each link, the bottom histogram shows the average total daily counts for each month.

where $\mathbf{R}_p$ is the vector location of the meteor with respect to p, and $\mathbf{R}_m$ is the vector of receiver m with respect to the meteor; $\mathbf{k}_i = k\mathbf{R_p}/|\mathbf{R}_p|$ and $\mathbf{k}_s = k\mathbf{R_m}/|\mathbf{R}_m|$ are the incident and scattered wavevectors, $k = 2\pi/\lambda$, λ is the radar wavelength, and $\mathbf{u} = (u,v,w)$ is the wind velocity vector that advects the meteor trail. The zonal (u), meridional (v) and vertical (w) components of the wind are positive to the east, north and up, respectively.

Given these definitions, the phase of the cross-correlation of voltages due to transmitters p and q of signals at receiver m evaluated at time lag τ (i.e., phase of $V_{mp}(t+\tau)V_{mq}^*(t)$), is given by

$$
\begin{aligned}
\phi_{mp,mq}(\tau) &= -(\mathbf{k}_i - \mathbf{k}_s)\cdot\mathbf{u}\tau - \mathbf{k}_i\cdot\mathbf{R}_p - \mathbf{k}_s\cdot\mathbf{R}_m + \mathbf{k}_i\cdot\mathbf{R}_q + \mathbf{k}_s\cdot\mathbf{R}_m \\
&= \mathbf{k}_B\cdot\mathbf{u}\tau + \mathbf{k}_i\cdot\Delta\mathbf{r}_{pq}
\end{aligned}
\tag{2}
$$

where $\mathbf{k}_B = \mathbf{k}_s - \mathbf{k}_i$ is the Bragg vector, $\mathbf{R}_p - \mathbf{R}_q = -\Delta\mathbf{r}_{pq}$, $\Delta\mathbf{r}_{pq} = \mathbf{r}_p - \mathbf{r}_q$, and $\mathbf{r}_p$ and $\mathbf{r}_q$ are the vector positions of transmitting antennas p and q respect to a common reference, respectively.

Inspecting equation (2), interferometric information $\mathbf{k}_i$ can be obtained from the cross-correlation at $\tau = 0$ for all 10 different interferometric pairs. The overall solution is obtained with a combination of beamforming and least square fitting (e.g., Chau & Clahsen, 2019, for details). The Doppler information (f_d) can be obtained from the auto-correlation at different temporal lags. The magnitude of $\mathbf{R}_i$ is obtained from the total range information, the vector difference between the receiver and transmitter positions, and $\mathbf{k}_i$ (e.g., Stober & Chau, 2015, equation (1)). Note that in MISO configurations one measures the angle of departure (AOD or in our case $\mathbf{k}_i$), while in more traditional SIMO systems (single transmitter, multiple receivers), the measured quantity is the angle of arrival (AOA, or $\mathbf{k}_s$).

Traditionally MLT wind products from SMRs have been obtained from a straightforward binning of meteor detections in altitude (z) and time (t) with resolutions Δh and Δt, respectively. Then a mean $\mathbf{u}_0(z,t) = (u_0(z,t),v_0(z,t),w_0(z,t))$ was obtained by solving $N_m(t,z)$ sets of equations as

$$
\mathbf{k}_{Bi}\cdot\mathbf{u}_0(z,t) = 2\pi f_{di}
\tag{3}
$$

where $\mathbf{k}_{Bi}$ and f_{di} are the Bragg vector and Doppler shift of detection i in the $N_m(t,z)$ set. The solution of this method is assumed to represent an average of the true wind field

over the horizontal region sample. Equivalently, the wind field is assumed homogeneous over the sampled region. The solution under these assumption is obtained using a doubly iterated weighted least square fitting approach. In the first fitting, the Doppler uncertainties are used as weights, while in the second run detections with differences more than three times the standard deviation are not considered, and the absolute differences are used as weights. The latter is implemented to propagate uncertainties to $\mathbf{u}_0$ considering not only the uncertainties in Doppler estimation, but also geophysical variability. The estimates using equation (3) are labeled below as M1 (method 1 or homogeneous).

The homogeneous method estimates mean winds within the radar illuminated area of ∼400 km diameter, and has been employed for many decades to study large-scale dynamics of MLT winds (i.e., planetary waves, and tides), either using single SMR stations (e.g., Hoffmann et al., 2007) or using multiple SMR stations to get wavenumber information (e.g., Manson et al., 2009; He & Chau, 2019). However, wind dynamics with smaller scales (time scales less than a few hours, horizontal scales less than 400 km, and vertical scales less than four kilometers) are expected to be filtered out with M1.

In this study, we take advantage of additional multistatic count statistics and more importantly the multistatic geometry's inherent provision of different viewing angles to implement two other new methods yielding wind fields with horizontal information: (a) a gradient method (M2), and (b) a method that uses inverse theory (M3).

3.1 Gradient method

In the gradient method, the wind field inside the observed volume is approximated by its first-order Taylor expansion terms, i.e.,

$$\begin{aligned}
\mathbf{u}(x,y,z,t) &\approx \mathbf{u}_0 + \frac{d\mathbf{u}}{dx}(x-x_0)\frac{d\mathbf{u}}{dy}(y-y_0) + \frac{d\mathbf{u}}{dz}(z-z_0) \\
&\approx \mathbf{u}_0 + \mathbf{u}_x(x-x_0) + \mathbf{u}_y(y-y_0) + \mathbf{u}_z(z-z_0)
\end{aligned} \tag{4}$$

where (x_0, y_0, z_0) is a reference point, (x, y, z) is the location where the velocity is evaluated, and

$$\begin{aligned}
\mathbf{u}_x &= (du/dx, dv/dx, dw/dx) \\
\mathbf{u}_y &= (du/dy, dv/dy, dw/dy) \\
\mathbf{u}_z &= (du/dz, dv/dz, dw/dz)
\end{aligned}$$

The positions (x, y, z) are calculated in kilometers taking into account latitude, longitude, and altitude of each detection and the Earth's radius at the reference point. The gradient approximation in spherical coordinates can be found in appendix A of Chau et al. (2017).

Using $\mathbf{u}(x,y,z,t)$ from equation (4) in equation (3) instead of $\mathbf{u}_0(z,t)$, the mean values (u_0, v_0, w_0) and the gradients of the horizontal wind components $(u_x, u_y, u_z, v_x, v_y, v_z)$ are obtained from solving the set of $N_m(t,z)$ equations

$$\mathbf{k}_{Bi} \cdot \mathbf{u}(x,y,z,t) = 2\pi f_{di} \tag{5}$$

As in the case of M1, the solutions are found using a doubly iterated weighted least square fitting. However, note that in the multistatic case we fit for nine parameters instead of three, so more detections than for M1 are required. In this work we have not fitted for the gradients of w, i.e., dw/dx, dw/dy, dw/dz, but this can be done in future work.

Similar gradient analysis approaches have been applied in the lower atmosphere (e.g., Browning & Wexler, 1968; Waldteufel & Corbin, 1979) and thermosphere (e.g., Conde & Smith, 1998; Meriwether et al., 2008). However, since most of these previous efforts were applied to monostatic systems, the relative vorticity (see below) was not measured

directly. Instead, this parameter was usually derived assuming local time and longitude were interchangeable (e.g., Burnside et al., 1981).

Following meteorological terminology (e.g., Wallace & Hobbs, 2006, Chapter 7), the horizontal gradient terms of the horizontal components can be combined to obtain

$$\nabla_H \cdot \mathbf{u} \quad = \quad u_x + v_y \qquad \text{Horizontal divergence} \tag{6}$$
$$\zeta \quad = \quad v_x - u_y \qquad \text{Relative vorticity} \tag{7}$$
$$\text{Stretching deformation} \quad = \quad u_x - v_y \tag{8}$$
$$\text{Shearing deformation} \quad = \quad v_x + u_y \tag{9}$$

We have implemented expressions for horizontal divergence and relative vorticity that take into account the latitude information (see e.g., Chau et al., 2017, equations (A15) and (A16), respectively). Due to the SIMONe Peru low latitude location (12°S), the results do not vary much as a function of latitude, so this information is not included.

We note that M2 improves on M1 analysis by providing spatial information of the wind field inside the observed volume. However, small structures would be smoothed out, as this information would be in the second and higher order terms if Taylor expansion was further extended. In addition, M2 approaches can introduce artificial structure, and is particularly true for regions with few or noisy measurements.

3.2 Regularized wind field inversion method

In order to explore smaller spatial scales that could be filtered out in M2 (see previous) and to avoid generation of artificial structures due to noisy measurements, in this work we have implemented a third approach (M3). M3 is an extension of the Harding et al. (2015) method, which was previously applied to a network of Fabry-Perot Interferometers to measure thermospheric wind fields. This technique uses inverse theory to find the smoothest field that matches the measurements to within their average uncertainties, instead of assuming an *a priori* functional form of the wind field. In this study's context, we solve a set of equations given by equation (5) where the unknown quantities are the values of the wind on every pixel in a high resolution grid. Regularization is needed since without it the problem is vastly under-determined and therefore unstable, as there are more unknowns than measurements.

Written in an optimization problem and following the nomenclature of Harding et al. (2015), the problem reduces to

$$\text{minimize} \qquad r(\bar{u})$$
$$\tag{10}$$
$$\text{such that} \qquad \|\Sigma^{-1/2}(A\bar{u} - \bar{d})\|_2^2 \leq \epsilon$$

where $\bar{u}$ is the vector of wind components at each gridded point (x_j, y_j, z_j), A is the matrix containing the corresponding components of Bragg vector (k_{Bi}), $\bar{d}$ is the vector containing the Doppler measurements (i.e., $2\pi f_{di}$), $\|\cdot\|_2^2$ is the vector 2-norm, Σ is the measurement covariance matrix, ϵ is a tuning parameter, and $r(\bar{u})$ is a scalar-valued non-negative function that measures the roughness of the wind field. In this work we have considered only a curvature regularization setting $r(\bar{u}) = \|C\bar{u}\|_2^2$ (e.g., Harding et al., 2015, equations 6, 7, and 8). Similar curvature operators have been used in other physically appropriate applications that estimate vector fields (e.g., Hysell et al., 2014; Nicolls et al., 2014; Stober et al., 2018). Other regularization conditions are also possible, e.g., the gradient regularization used by Harding et al. (2015), but given the large quantity of data offered by meteor radar systems, we chose a conservative approach (see below).

Then the minimization problem becomes

$$\text{minimize} \qquad \|\Sigma^{-1/2}(A\bar{u} - \bar{d})\|_2^2 + \lambda_0 \|C\bar{u}\|_2^2 \tag{11}$$

taking the form of a Tikhonov regularization. Solving equation (11) analytically (Aster et al., 2013), the solution $\bar{u}^*$ is

$$\bar{u}^* \quad = \quad [A^T \Sigma^{-1} A + \lambda_0 C^T C]^{-1} A^T \Sigma^{-1} \bar{d} \tag{12}$$

which can be computed using sparse matrix routines (e.g. "spsolve" from the Python "scipy" linear algebra package). More details and discussion on the implementation can be found in Harding et al. (2015).

Although the original implementation of Harding et al. (2015) was implemented at a single altitude, the extension to SIMONe data is trivial, since similar to M1 and M2, the input data is already binned into different altitudes and times. To keep some smoothness in time, equation (12) has been solved for overlapping times. In the examples presented in this work, $\bar{u}^*$ has been obtained using meteor detections in a time interval of $\Delta_t = 30$ minutes, but solutions are obtained on a 15 minute time cadence with spatial resolutions $\Delta_z, \Delta_x, \Delta_y$ at 2, 20, and 20 km, respectively. In altitude, a Gaussian weighting function with $\sigma = \Delta_z/2$ around the desired altitude $\pm 3\Delta_z/2$ has been applied.

As in any Tikhonov regularization problem, there is no single formula for selection of the optimal value of λ_0. In our case, we have first estimated λ_0 empirically using a generalized cross validation (GCV) approach using a few hours of data (e.g., Fenu et al., 2016) and then selected its median value for the examples shown in this work. In the larger context of an operational system, however, not only is using a GCV approach computationally expensive, but more importantly there is a huge variability in the λ_0 selection that results. Such variability is particularly problematic for our multistatic SMR systems, since the number of counts and diversity of Bragg vectors vary widely as function of time of the day. For example, the minimum counts occur around 2300 UT every day (see Figure 2).

For this work, we have preferred to take a conservative approach and use a median value ($\lambda_0 = 1000$) for all times and altitudes. This implies an intrinsic filtering (smoothing) of small scales that could be otherwise resolved using information embedded in the input data with a different regularization constraint value. Future efforts will concentrate on analysis with smaller λ_0 for appropriate selected times, as well as the extension of M3 to a fully 3D solution, instead of a 2D solution for selected altitude bins.

4 Wind results

In this section we present the preliminary MLT wind results obtained with SIMONe Peru using the analysis methods of section 3). We begin with examples of derived parameters using M1 and M2, then we show results of large scale features from M2 estimates, followed by examples of small scale features obtained with M3.

4.1 Mean winds and gradients of the horizontal wind

In all SMRs, the main products are mean horizontal winds obtained with M1 approaches. In Figure 4, we present seven days of mean winds obtained with M1 and M2 between December 9 and 16, 2019. The left/right column shows the zonal, meridional and vertical components of M1/M2. Both estimates have been obtained with one-hour and two-kilometer bins, and five-minute and 500-m sampling. From a simple visual inspection (and also from a point-to-point correlation not shown here), the zonal and meridional mean estimates with M1 and M2 are in excellent agreement. Both components show a typically expected dominant diurnal behavior with variability over time scales of a few days.

On the other hand, the mean vertical wind components produced by M1 and M2 are not in good agreement. However, both show relative large variability of a few meters per second.
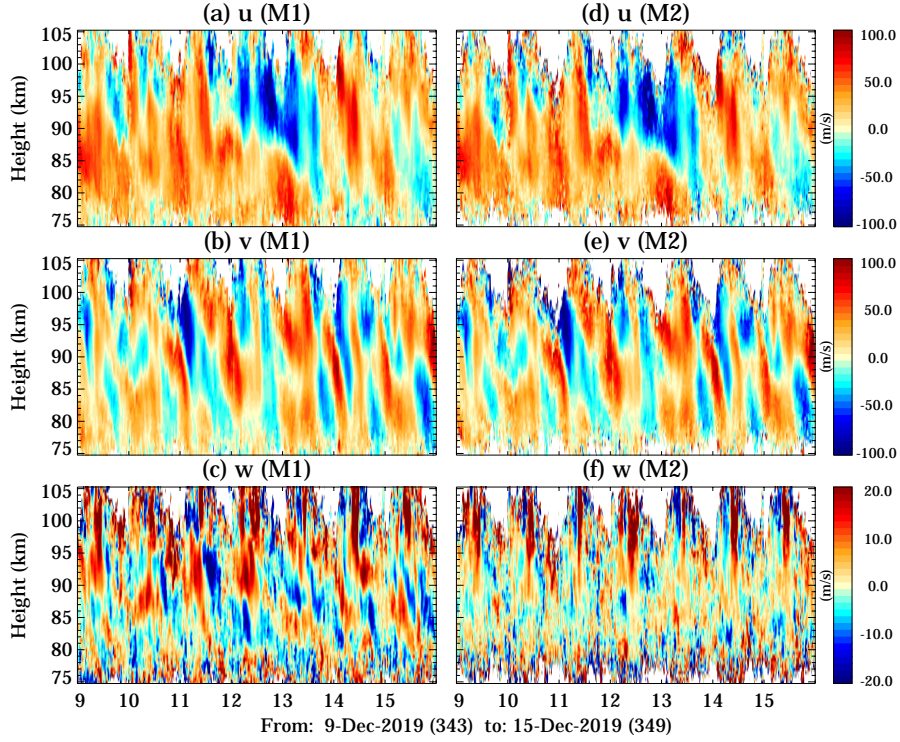
Figure 4. Mean 3D winds between December 9 and 16, 2019 obtained with: (left) homogeneous method (M1) and (b) gradient method (M2), in both cases using one hour and two kilometer bins.

Before discussing the discrepancies in vertical components, we show the gradient information of the horizontal components in Figure 5 using the same data, resolution and sampling used in Figure 4, i.e., (a) u_z, (b) Horizontal divergence ($\nabla_H \cdot \mathbf{u}$), (c) Stretching deformation, (d) v_z, (e) relative vorticity (ζ), and (f) shear deformation. In all six parameters the units are ms^{-1}km^{-1}.

All six parameters show large temporal and altitude variability with a dominant diurnal behavior. Features include (a) a large negative vertical gradient in the zonal component (u_z), accompanied by large positive shear deformation around December 13, and (b) a 24-hour period large oscillation in the horizontal divergence around December 12. The variability and magnitudes of these parameters, in particular estimates of horizontal gradients, are much larger and clearer than those reported over northern Norway (69°N) (e.g., Chau et al., 2017, Figure 4). A direct comparison is not relevant, since the latitudes and seasons are different, but we note that it is striking to see such variability over the equatorial Peru region.

Again from a visual inspection, we qualitatively find following Chau et al. (2017) that structures in the horizontal divergence (Figure 5b) resemble the structures in M1 vertical component (Figure 4c). This indicates that vertical velocities obtained with M1, at least over relative larger areas, are significantly contaminated by horizontal divergence as also found by Chau et al. (2017).

To get a more quantitative idea of vertical component correlations, in Figure 6 we show three 2D histograms using results between 82 and 92 km from Figures 4 and 5. Specifically, these show: (a) w (M1) vs w (M2), (b) Horizontal divergence vs. w (M2), and (c) Horizontal divergence vs. w (M1). The highest significant correlation is found, as expected,
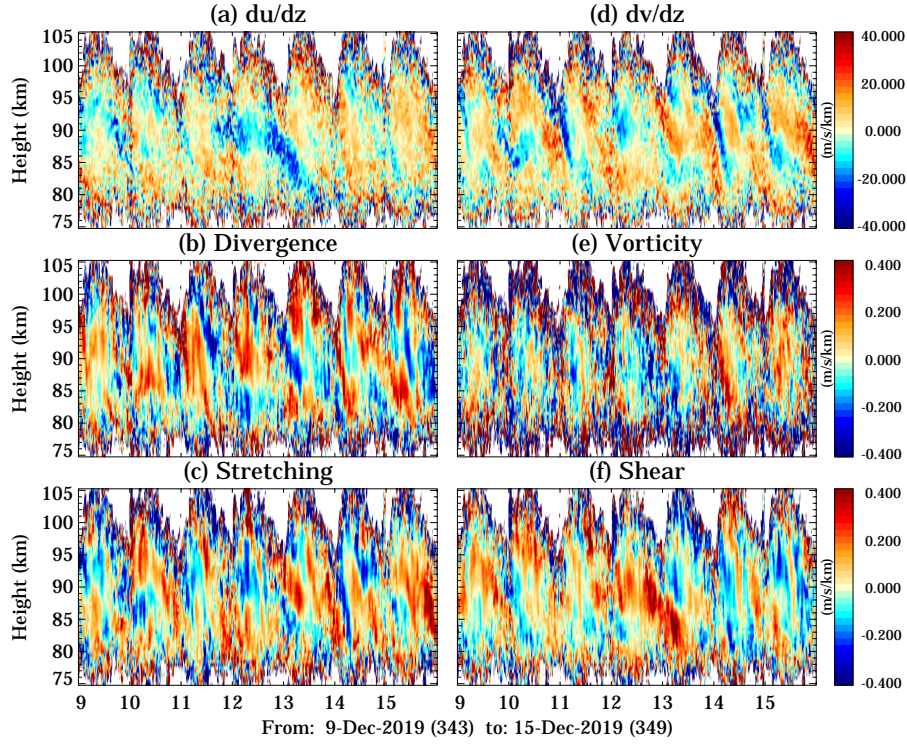
Figure 5. Derived components of horizontal winds with the gradient method (M2): (a) zonal wind vertical gradient, (b) Horizontal divergence, (c) stretching deformation, (d) meridional wind vertical gradient, (e) relative vorticity (ζ), (f) shear deformation, using the same period and sampling as in Figure 4.

between the horizontal divergence and w (M1), with a Pearson correlation coefficient of 0.64. If instead estimates obtained with four-hour and four-kilometer bins are used, the correlation coefficient is 0.78 (results not shown here). This indicates that the observed correlation between horizontal divergence and w is mainly due to structures with medium spatial (a few hundred of kilometers in the horizontal and more than 4 km in the vertical) and temporal (more than four hours) scales.
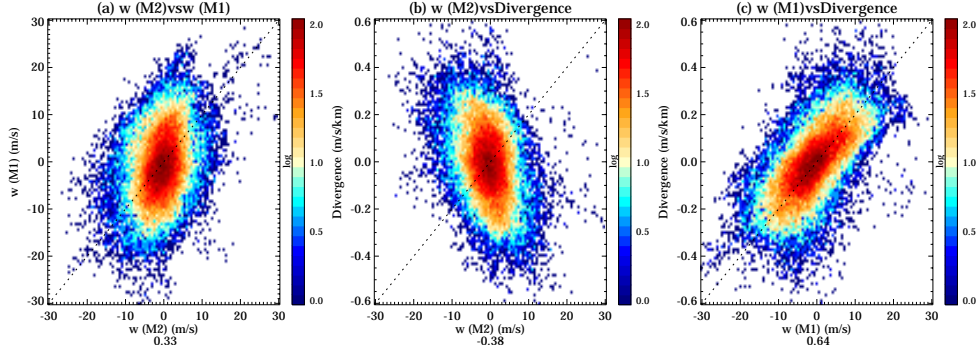

Figure 6. 2D histograms of vertical velocity estimates and horizontal divergence using the results between 82 and 92 km shown in Figures 4 and 5: (a) vertical estimates using M1 and M2, (b) vertical estimates using M2 (Figure 4f) and horizontal divergence (Figure 5b), and (c) vertical estimates using M1 (Figure 4c) and horizontal divergence. The Pearson correlation coefficient is indicated for each plot.

We have also estimated M2 parameters using four-hour and four-kilometer time-altitude bins. The results are included in the supplemental material in Figures S2 and S3, for the mean winds and gradients, respectively. These estimates represent detailed observations of the dynamics of large-scale processes.

4.2 Large-scales temporal features

In this section, we present an overview of large scale wind features that have been obtained with SIMONe Peru between October 2019 and March 2020. Note that although the results are not unique to multistatic configurations, our results confirm that mean horizontal wind components, in this case obtained with M2, are also useful for studies of large scale features.

Figure 7 shows 4-day averaged zonal and meridional winds and the total amplitudes of waves with selected key periods of 48, 24, 12, 12.42, and 8 hours, corresponding to the quasi-two day, diurnal, semidiurnal, quasi-lunar, and terdiurnal components, respectively. All of them have been obtained using a 21-day running window and a least-square fitting approach similar to the one used by Sandford et al. (2006). The selection of a 21-day window has been done to separate the quasi-lunar (12.42 h) and the semidiurnal (12 h) components. Both of these components were previously observed to have large amplitudes in the northern hemisphere MLT altitudes at both mid and high latitudes, particularly between January and February months (e.g., Chau et al., 2015; He & Chau, 2019).

The salient features in Figure 7 are: (a) strong planetary wave activity (with periods of a few days) in the mean zonal and meridional winds, (b) quasi-two day and diurnal components present the largest amplitudes, (c) quasi-lunar and terdiurnal components present the smallest amplitudes. In the case of quasi-two-day and diurnal components, the largest amplitudes are observed in the meridional component. These results
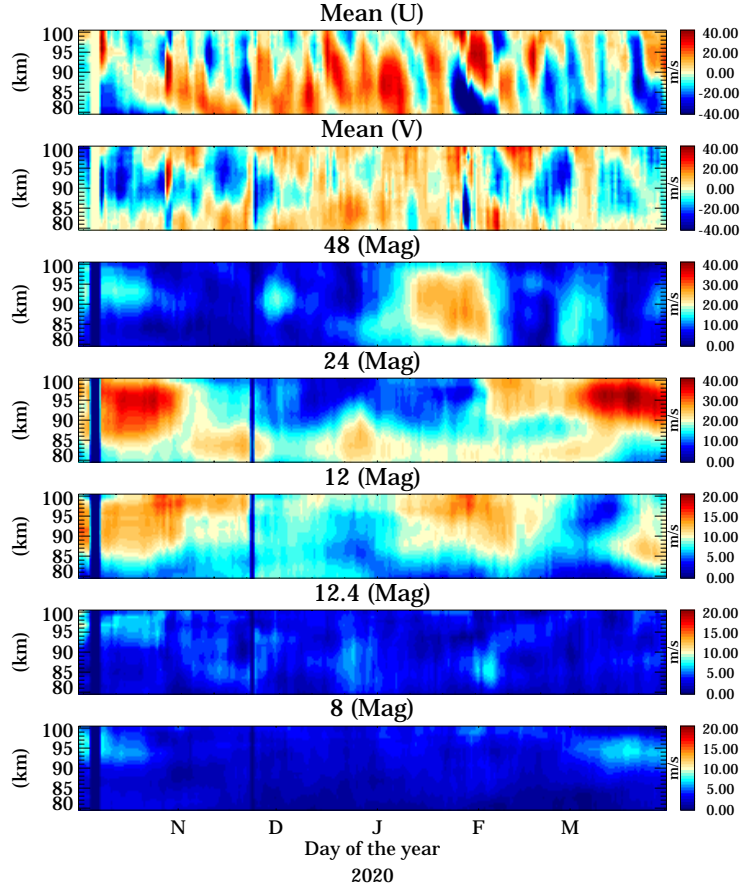
SIMONe Peru (12S)

Figure 7. Mean horizontal winds and selected waves components between October 2019 and March 2020: (a) mean zonal wind, (b) mean meridional wind, (c) quasi two-day wave, (d) total diurnal tide, (e) total semidiurnal tide, (f) quasi-lunar tide, and (g) total 8 hour components. In the case of the wave components, the total magnitude is shown, i.e., $\sqrt{u_T^2 + v_T^2}$. The mean zonal and meridional winds have been obtained with a 4-day running window, while the wave components used a 21-day running window (see text for details). Data gaps are shown with vertical yellow and dark blue narrow rectangles. Data gaps are shown with vertical yellow and dark blue narrow rectangles.

536 are in good agreement with previous low-latitude MLT studies (e.g., Rajaram & Gurubaran,
537 1998; Davis et al., 2013; Araújo et al., 2014).

4.3 Small-scales

539 Figure 5 already shows the benefits of SIMONe Peru's multistatic approach and
540 analysis by providing horizontal information within the observed area, in the form of hor-
541 izontal divergence, relative vorticity, deformation (stretching and shearing). In this sec-
542 tion, we further extend and improve this horizontal information by implementing M3 from
543 section 3.2 as the regularized inversion of Harding et al. (2015).

544 Figure 8 shows M3 resultant mean wind fields at three selected altitudes: 85, 89,
545 and 93 km. The first row shows the wind fields obtained with the gradient-based M2 method,
546 but using four-hour and four-kilometer time-altitude bins, to preserve representation of
547 medium and large scale features in structures with periods larger than 4 hours. The di-
548 rection and magnitude are indicated with arrows. The arrows are color coded in green
549 tones to help its visualization (upper right color bar). The contour gray lines indicate
550 the normalized meteor counts used in the inversion while the colored background indi-
551 cate the mean vertical velocity $w(M2)$ (middle color bar). The large black arrow cor-
552 responds to the mean horizontal wind using M2, i.e., (u_0, v_0), where 50 km represents
553 50 m/s. This mean vector and the contour gray lines are repeated in the lower two rows.

554 The second row shows the wind fields obtained with M3 (regularized inversion),
555 color coded as in the first row (upper color bar). This time the colored contours show
556 w obtained with M3 (middle colorbar). The M3 estimates have been obtained with res-
557 olutions of $\Delta z = 2$ km, $\Delta x = \Delta y = 20$ km, and $\Delta t = 30$ minutes. To avoid showing
558 data with small counts and relative large zenith angles, only estimates with enough counts
559 and within 120 km horizontal radius over the transmitter station, are shown. Note that
560 most estimates at large zenith angles suffer from precision issues and from poor Bragg
561 vector diversity. The precision issue is a well known feature of SMR with interferome-
562 try, where the zenith angle precision decreases with zenith angle, and therefore there is
563 a large uncertainty on altitude as cited by previous studies (Holdsworth, 2005; Hocking,
564 2018; Vaudrin et al., 2018). The poor vector diversity issue reduces to an equivalent ob-
565 servation of those regions with a monostatic system.

566 In general, results show a reasonable agreement between M2 and M3 horizontal com-
567 ponents. Differences are expected due to different averaging and to different conceptual
568 implementation. In particular, in M2 we use a functional form that smooths small fea-
569 tures, while in M3 the inversion algorithm implements smoothness regularization. In the
570 former, one can control the amount of regularization by adjusting λ_0. As a reminder, these
571 results have been obtained with a conservative regularization value, independent of the
572 underlying data's number of counts or Bragg vector diversity (see above).

573 In the third row, we show the M3 estimates but with the mean values from M2 sub-
574 tracted, through subtracting the (u_0, v_0, w_0) M2 value. Recall that these mean values
575 are obtained with a four-hour and four-kilometer bin, which allows subtraction of large
576 scale features. In this plot row, the vectors of the horizontal wind are color-coded with
577 the lower left color bar. The visualization attempts to remove large scale features such
578 as tides or waves with periods greater than 4 hours that are contained in M2 estimates,
579 yielding a representation of smaller scales. From examining the vertical velocity color
580 contours, spatial structures of 100 km or so are evident. In the case of the horizontal wind
581 vector, results show a mix of different flow configurations at the three altitudes: shear
582 flow with curvatures, small vortices, convergent flows, and related structures.

583 Although we are confident of the general good performance of our regularized in-
584 version approach, we emphasize that the approach taken here remains conservative and
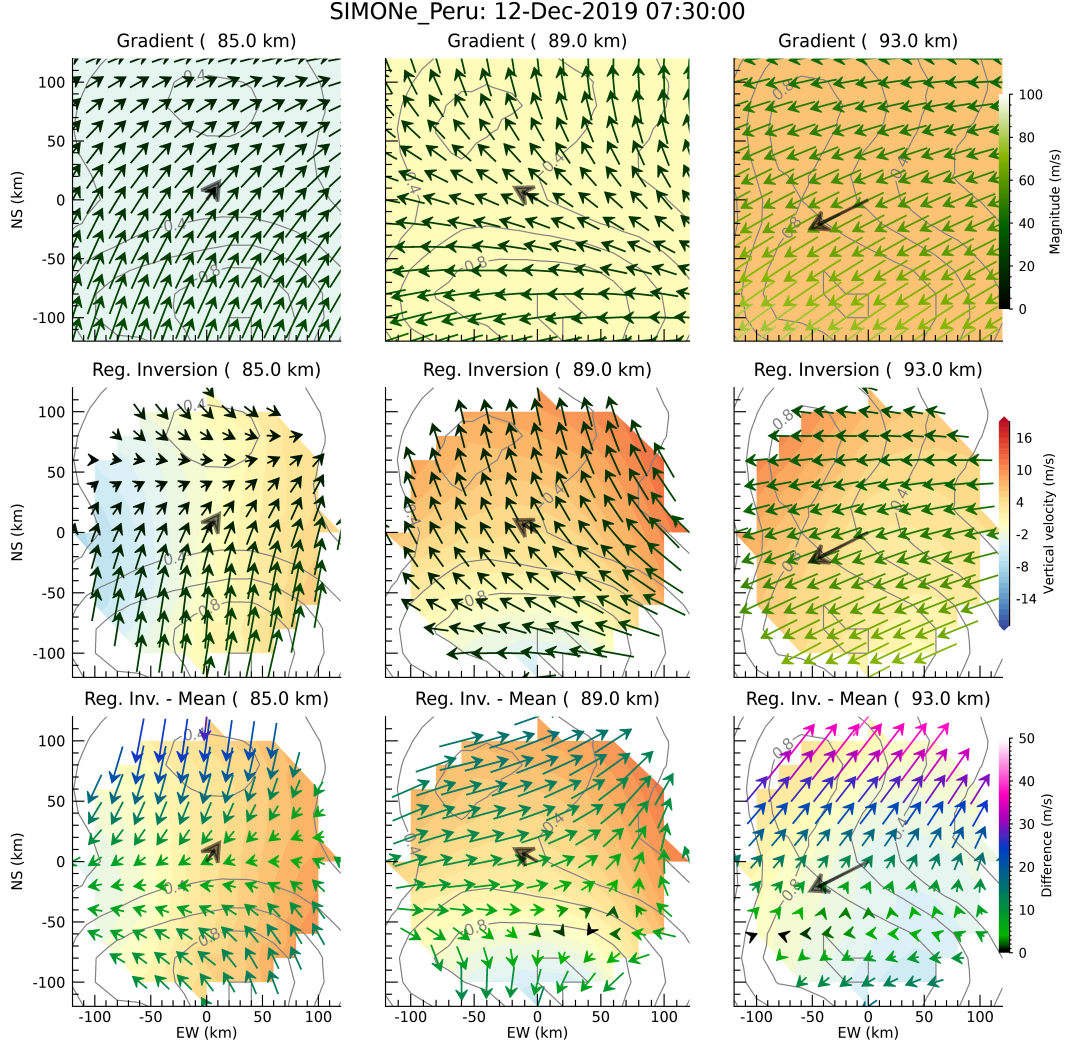
Figure 8. Wind estimates for selected heights on December 12th, 2019 at 0730: (first column) 85 km, (second column) 89 km, and (third column) 93 km. The first row shows the horizontal wind field obtained with the gradient method (M2) using four-hour and four-kilometer bins; the second row shows the horizontal wind field obtained with a regularized inversion (M3); and the third row shows the wind field difference between the values in the second row and the mean horizontal wind (M2) indicated in all panels with a black arrow. In all cases the normalized meteor counts are indicated as gray contour lines, while the color contour represent the vertical component from M2 (first row), M3 (second row), and M3-M2 (third row). The color bars for the arrows representing vector fields are located to the right of each row (see text for more details).

585 does not in particular assert that the M3 approach is necessarily superior in all situa-
586 tions.

587   For further information on results obtained with the M3 approach, the supplemen-
588 tal material includes a movie of wind field frames obtained every 15 minutes between De-
589 cember 11 and 13, 2019. We have selected this time period due to: (a) good coverage
590 with all five receiving stations (Figure 2), (b) diurnal tide amplitude that is smaller at
591 the upper altitudes (Figure 7), and (c) large localized variability in derived parameters
592 from horizontal gradients of the horizontal wind components (Figure 5). In general, the
593 observed features in the third row supplemental plots appear to be of geophysical na-
594 ture in all three components. However, clear examples of questionable results are observed
595 around 2300 UT, when the meteor count statistics are relatively smaller (Figure 2).

5 Non-wind results

597   Although the focus of this study is primarily on MLT winds, we briefly show in this
598 section that SIMONe Peru is also able to detect other echoes with relatively large radar
599 cross sections. One of the obvious application targets are airplanes (not shown here) that
600 in pulsed systems could be range aliased due to radar ambiguity issues. In our case, the
601 coded-CW implementation inherently provides very clean range-Doppler ambiguity char-
602 acteristics, and our effective maximum unambiguous total range in our standard anal-
603 ysis is 6000 km.

604   Other low-latitude geophysical echoes with strong cross-sections that are routinely
605 observed with SIMONe Peru include: (a) daytime EEJ echoes (e.g., Farley, 2009), (b)
606 nighttime EEJ echoes (e.g., Hysell & Chau, 2002), (c) non-specular meteor echoes (Chapin
607 & Kudeki, 1994), and (d) strong meteor-head echoes (e.g., Chau & Woodman, 2004).
608 Figure 9 shows a range-time intensity (RTI) and spectrogram of decoded signals (inco-
609 herently integrated among interferometric channels) taken on April 16 at 01:01:48 UT
610 with the JRO-Azpitia link. Besides some specular meteor echoes employed for MLT wind
611 observations, we observed: (a) nighttime EEJ echoes around 240 km, accompanied by
612 a narrow spectra centered at zero frequency, (b) a long-lasting non-specular meteor trail
613 around 460 km lasting for more than one minute, with different Doppler shifts depend-
614 ing on total range (negative at closer range, positive at further ranges), and (c) shorter-
615 lived non-specular echoes at different ranges and times.

616   Strong non-specular echoes observed at relatively small zenith angles ($< 20°$) can
617 also be employed to derive MLT wind profiles (e.g., Oppenheim et al., 2009). Similarly,
618 wide beam observations of daytime and night EEJ echoes can be routinely obtained over
619 the middle point of each link. The current SIMONe Peru configuration would allow these
620 observations simultaneously over five different locations, enabling studies of spatial EEJ
621 diversity.

622   The non-specular echoes, particularly those with strong and long-lasting features,
623 can be also used to determine the atmospheric entry location of the bolide that gener-
624 ates the echoes, and perhaps even its trajectory when they are observed with multiple
625 views at relative small zenith angles ($< 20°$). Figure 10 shows a zoomed version of the
626 long-lasting event showed in Figure 9 with JRO-Azpitia, but also the RTIs with JRO-
627 Huancayo and JRO-Santa Rosa. Note that echoes are weaker in the JRO-Santa Rosa
628 link not for geophysical reasons but due to a failure in the front-ends (AFEs) of one of
629 the linearly polarized receiving channel. Using the total range information provided by
630 these three links, we were able to estimate the entry point of the bolide that created the
631 echoes as 14.1808°S, 76.8774°W, 96654 m. These location is in excellent agreement with
632 visual observations.

633   These events have been obtained directly from the raw data files using only the read-
634 ing and decoding blocks, and therefore have not been processed with our routine RSP.
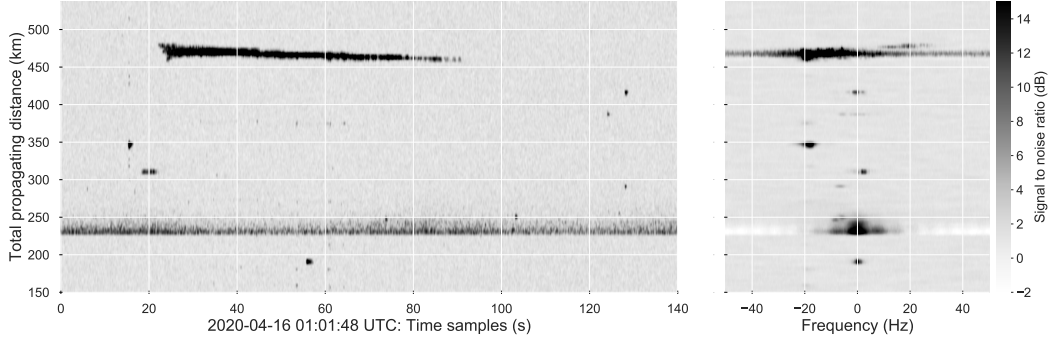
Figure 9. (left) Range time intensity (RTI) and (right) spectrogram for a selected period of 140 seconds on April 16 01:01:48 UT obtained with the JRO-Azpitia link. Besides the sporadic specular meteor echoes, non-specular meteor echoes are observed above 450 km lasting more than a minute and nighttime EEJ echoes are observed around 230-250 km.
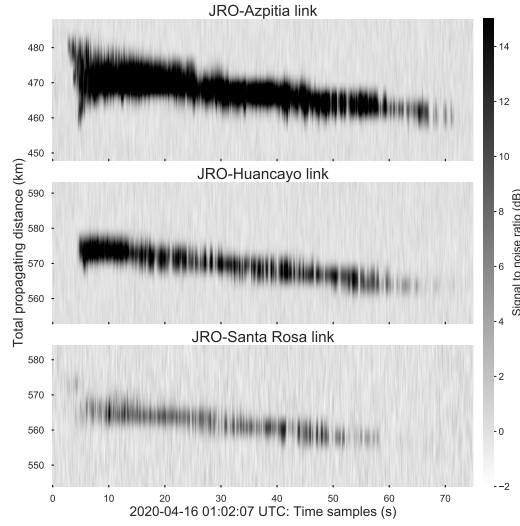

Figure 10. RTI of the strong non-specular echo shown in Figure 9, but over three bistatic links: JRO-Azpitia, JRO-Huancayo, and JRO-Santa Rosa.

Once the signals are decoded, the rest of the analysis is similar to pulse-pulse analysis used in many coherent radars, like the so-called Mesosphere-Stratosphere-Troposphere (MST) radars (Woodman & Guillén, 1974). In principle, one would need to add new detection and estimation boxes to work in parallel to our routine RSP, but this is straightforward due to the SIMONe architecture.

Probing further yields several interesting features of this bolide event. We used a special range-Doppler matched filter analysis to treat the length of each baud as the effective IPP (i.e., 10 μs). Through subsequent use of matched filter decoding (1000 bauds), we were then also able to detect the meteor-head echo created by the ablating plasma in front of the bolide as having radial velocity close 6 km/s (1.2 kHz/s spectral motion). The output of the range-Doppler matched filter bank analysis, providing echo power as a function of time and range is shown in Figure 11. In this figure, the head echo corresponding to the plasma surrounding the ablating meteoroid is visible moving from 470 to 460 km distance near 01:02:11 UTC, followed by the longer lived trail echoes formed after the pass of the meteoroid shown in Figure 10. Figure 12 shows further analysis from this data producing estimated range and range-rate for the head echo. This analysis, although computationally intensive, is useful to avoid range and frequency ambiguities. This approach has a maximum unambiguous range which remains at 6000 km, with range-aliasing converted into an increase of flat noise by the pseudo random nature of the code, and an unaliased Doppler extent of ±230 km/s (Nyquist frequency = 50 kHz). We note that a very similar approach has been applied successfully to E region plasma irregularity studies using the radar aurora system called ICEBEAR (e.g., Huyghebaert et al., 2019).
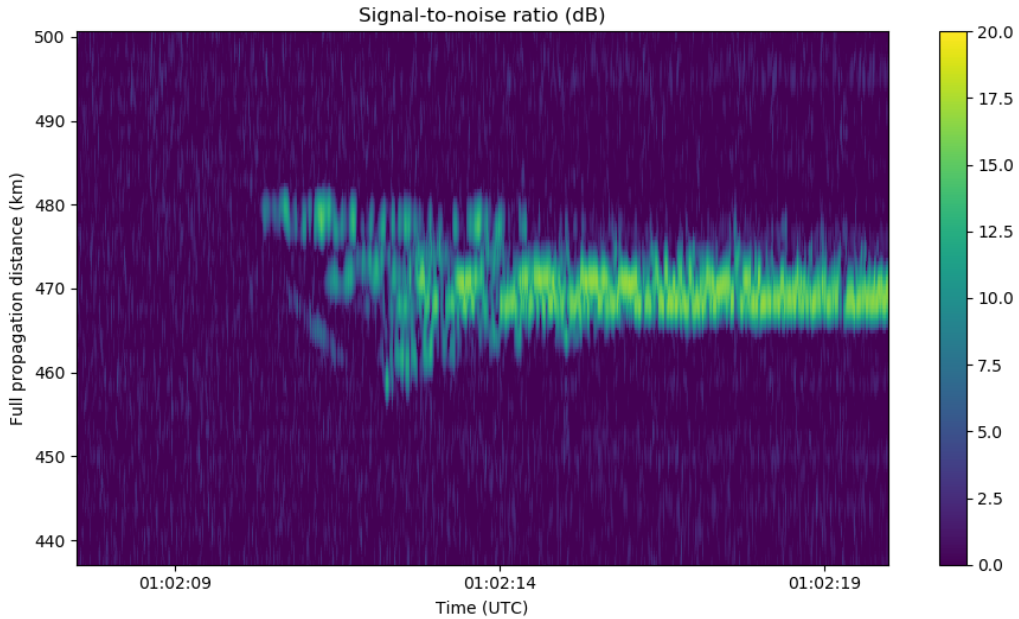

Figure 11. Range-Doppler matched filterbank output for the Peru bolide.

6 Concluding Remarks

We have shown in this paper that SIMONe Peru has been successfully implemented for studies of MLT dynamics at low latitudes at different scales. The typical large scale features studied with monostatic SMRs are clearly observed with the system. However, since the horizontal scales of these features are much larger than the observed area, new
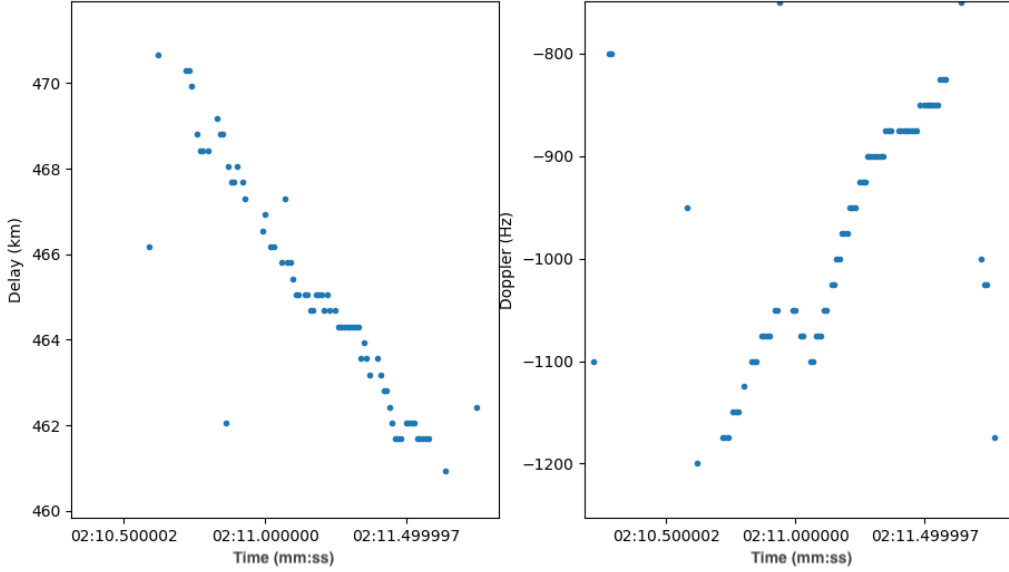
Figure 12. Range and Doppler shift estimated for the bolide head echo. Note that the times are indicated in minutes (mm) and seconds(ss), i.e., mm:ss with respect to April 16th 2020 01 hour.

662 and exciting contributions at these scales can be provided by future coordinated obser-
663 vations that complement SIMONe Peru measurements with other existing ground-based
664 radars (like those from Brazil, India, Indonesia) (Rajaram & Gurubaran, 1998; Araújo
665 et al., 2014; Rao et al., 2014). These coordinated observations have considerable poten-
666 tial for separation of the space-time features of tides and planetary waves, similar to He
667 and Chau (2019).

668   In the case of medium scales, one of the direct contributions of multistatic systems
669 such as SIMONe Peru lies in improved estimation of the vertical velocity when using rel-
670 ative large areas, by estimating the horizontal gradients of the horizontal wind, i.e., w
671 (M2). If the number of detections are sufficient, vertical velocities with less horizontal
672 divergence contamination can be estimated when smaller areas are used. This narrow
673 region approach has been implemented to study the vertical velocities of planetary waves
674 at times of maximum meteor counts occurring only a few hours per day (e.g., Babu et
675 al., 2012; Egito et al., 2016). We have implemented such approach using an area with
676 40 km radius, and indeed the resulting w (M1) and w (M2) estimates are in excellent
677 agreement (results not shown here). Future work will provide focused study of vertical
678 velocities obtained with M2 and M3 and their observed large variability and relative large
679 amplitudes, leading to implications for the dynamics and electrodynamics of the equa-
680 torial MLT and the E-region dynamo regions.

681   With the gradient method (M2), we are now able to characterize wind fields over
682 the observed area with nine parameters instead of the traditional three parameters (u_0,
683 v_0, w_0). A simple extension of this method could be done by including higher order terms
684 or even cross terms. However, we have preferred to use a method at present that uses
685 inverse theory and Tikhonov regularization. As in any inverse theory problem, there are
686 different ways to approach the under determined problem. In this study, we have extended
687 the method of Harding et al. (2015) with encouraging results despite the conservative
688 approach we have taken (use of a single λ_0 for all cases). However, we plan to extend
689 this method further in the future to consider a true 3D solution (and not 2D solutions

for different altitude cuts). This will include an adaptive selection of the regularizing factor λ_0 that takes into account the data sampling and Bragg vector diversity variables. On top of these improvements, we expect that M3 would definitely outperform M2 as more links, including MIMO links, are added, since this allows not only more count statistics but also more Bragg vector diversity. The resulting structure information scales naturally with the information provided in the data.

Although not included in this work, the SIMONe Peru data can also address smaller scales in neutral motions on a statistical basis, by using the second-order statistics of line-of-sight velocities. For example, average momentum fluxes can be obtained using zero-lag second-order statistics (e.g., Hocking, 2005). The method has been applied with varying degrees of success using monostatic SMRs. Slight improvements have been obtained using a bistatic approach by Spargo et al. (2019). Recently, Vierinen et al. (2019) has extended the concept to use non-zero spatial and temporal lags. This allows the exciting and information-rich possibility of statistical estimation of correlation, structure and spectral functions of kinetic energy and momentum flux at different spatial and temporal scales.

Furthermore, SIMONe data from specular echoes could also be used to measure temperature, neutral density and meteor orbits as has been done with monostatic systems (e.g., Hocking et al., 2001; Holdsworth et al., 2004; Tsutsumi et al., 1999). In addition with some software improvements, SIMONe data can also be used to routinely observe strong coherent VHF radar echoes as presented by the example here. In particular, for the case of SIMONe Peru, we have shown examples of day and nighttime EEJ, non-specular meteor and meteor-head echoes. The latter echoes could be used to detect bolides as our initial analysis demonstrated.

Finally, SIMONe Peru is centered at the multifaceted JRO complex, where multiple-technique and multi-instrument campaigns could be implemented in the future for cross-validation purposes and, more importantly, to study processes that are difficult to address with a single instrument or technique. One of such future campaigns could target the simultaneous use of JRO's different observational modes: MST (60-85 km winds) (Lee et al., 2019), oblique daytime EEJ (95-110 km zonal winds) (Shume et al., 2005), non-specular meteor echoes (90-110 km horizontal winds) (Oppenheim et al., 2009), and optical remote sensing instruments, e.g., Near Infrared Airglow Camera on the International Space Station or the Michelson Interferometer for Global High-resolution Thermospheric Imaging on the ICON NASA explorer (e.g., Harding et al., 2017).

References

Abdu, M. A., Brum, C. G., Batista, P. P., Gurubaran, S., Pancheva, D., Bageston, J. V., ... Takahashi, H. (2015, 1). Fast and Ultrafast Kelvin wave

modulations of the equatorial evening f region vertical drift and spread f development Aeronomy. *Earth, Planets and Space*, *67*(1), 1. Retrieved from http://www.earth-planets-space.com/content/67/1/1 doi: 10.1186/s40623-014-0143-5

Andrioli, V. F., Fritts, D. C., Batista, P. P., & Clemesha, B. R. (2013). Improved analysis of all-sky meteor radar measurements of gravity wave variances and momentum fluxes. *Annales Geophysicae*, *31*(5), 889–908. Retrieved from https://www.ann-geophys.net/31/889/2013/ doi: 10.5194/angeo-31-889-2013

Araújo, L. R., Lima, L. M., Batista, P. P., Clemesha, B. R., & Takahashi, H. (2014). Planetary wave seasonality from meteor wind measurements at 7.4Â° S and 22.7Â° S. *Annales Geophysicae*, *32*(5), 519–531. Retrieved from https://www.ann-geophys.net/32/519/2014/ doi: 10.5194/angeo-32-519-2014

Aster, R. C., Borchers, B., & Thurber, C. H. (2013). *Parameter Estimation and Inverse Problems.* doi: 10.1016/C2009-0-61134-X

Babu, V. S., Ramkumar, G., & John, S. R. (2012, 4). Seasonal variation of planetary wave momentum flux and the forcing towards mean flow acceleration in the MLT region. *Journal of Atmospheric and Solar-Terrestrial Physics*, *78-79*(C), 53–61. doi: 10.1016/j.jastp.2011.05.010

Browning, K. A., & Wexler, R. (1968). The determination of kinematic properties of a wind field using {Doppler} radar. *J. Appl. Meteorol.*, *7*(1), 105–113. doi: 10.1175/1520-0450(1968)007{\$}⟨{\$}0105:TDOKPO{\$}⟩{\$}2.0.CO;2

Burnside, R. G., Herrero, F. A., Meriwether, J. W., & Walker, J. C. G. (1981). Optical observations of thermospheric dynamics at Arecibo. *Journal of Geophysical Research*, *86*, 5532–5540.

Chapin, E., & Kudeki, E. (1994). Radar Interferometric Imaging Studies of Long-Duration Meteor Echoes Observed at {Jicamarca}. *J.˜Geophys.˜Res.*, *99*, 8937–8949.

Chau, J. L., & Clahsen, M. (2019). Empirical phase calibration for multi-static specular meteor radars using a beam-forming approach. *Radio Science*. doi: 10.1029/2018RS006741

Chau, J. L., Fejer, B. G., & Goncharenko, L. P. (2009, 3). Quiet variability of equatorial {ExB} drifts during a sudden stratospheric warming event. *Geophys. Res. Lett.*, *36*(5), 1–4. doi: 10.1029/2008GL036785

Chau, J. L., Goncharenko, L. P., Fejer, B. G., & Liu, H. L. (2012, 6). Equatorial and Low Latitude Ionospheric Effects During Sudden Stratospheric Warming Events. *Space Science Reviews*, *168*, 385.

Chau, J. L., Hoffmann, P., Pedatella, N. M., Matthias, V., & Stober, G. (2015). Upper mesospheric lunar tides over middle and high latitudes during sudden stratospheric warming events. *Journal of Geophysical Research: Space Physics*, *120*(4), 3084–3096. Retrieved from https://agupubs.onlinelibrary.wiley.com/doi/abs/10.1002/2015JA020998 doi: 10.1002/2015JA020998

Chau, J. L., Stober, G., Hall, C. M., Tsutsumi, M., Laskar, F. I., & Hoffmann, P. (2017). Polar mesospheric horizontal divergence and relative vorticity measurements using multiple specular meteor radars. *Radio Science*, *52*(7), 811–828. Retrieved from http://dx.doi.org/10.1002/2016RS006225 doi: 10.1002/2016RS006225

Chau, J. L., Urco, J. M., Vierinen, J. P., Volz, R. A., Clahsen, M., Pfeffer, N., & Trautner, J. (2019). Novel specular meteor radar systems using coherent MIMO techniques to study the mesosphere and lower thermosphere. *Atmospheric Measurement Techniques*, *12*, 2113–2127. doi: 10.5194/amt-12-2113-2019

Chau, J. L., & Woodman, R. F. (2004). Observations of Meteor-Head Echoes Using the {Jicamarca 50 MHz} Radar in Interferometer Mode. *Atmos. Chem. Phys.*, *4*, 511–521.

Conde, M., & Smith, R. W. (1998). Spatial structure in the thermospheric horizontal wind above {Poker Flat, Alaska}, during solar minimum. *J. Geophys. Res.*, *103*, 9449–9472. doi: 10.1029/97JA03331

Davis, R. N., Du, J., Smith, A. K., Ward, W. E., & Mitchell, N. J. (2013). The diurnal and semidiurnal tides over Ascension Island (° S, 14° W) and their interaction with the stratospheric quasi-biennial oscillation: Studies with meteor radar, eCMAM and WACCM. *Atmospheric Chemistry and Physics*, *13*, 9543–9564. doi: 10.5194/acp-13-9543-2013

Egito, F., Andrioli, V. F., & Batista, P. P. (2016). Vertical winds and momentum fluxes due to equatorial planetary scale waves using all-sky meteor radar over Brazilian region. *Journal of Atmospheric and Solar-Terrestrial Physics*, *149*, 108–119. doi: 10.1016/j.jastp.2016.10.005

England, S. L. (2012). A Review of the Effects of Non-migrating Atmospheric Tides on the Earth's Low-Latitude Ionosphere. *Space Science Reviews*, *168*, 211–236.

Ester, M., Kriegel, H.-P., Sander, J., & Xu, X. (1996). A Density-Based Algorithm for Discovering Clusters in Large Spatial Databases with Noise. In *Kdd'96: Proceedings of the second international conference on knowledge discovery and data mining* (pp. 226–231). Retrieved from `www.aaai.org`

Farley, D. T. (2009). The equatorial E-region and its plasma instabilities: a tutorial. *Ann. Geophys*, *27*, 1509–1520.

Fejer, B. G., Olson, M. E., Chau, J. L., Stolle, C., Lühr, H., Goncharenko, L. P., ... Nagatsuma, T. (2010, 8). Lunar-dependent equatorial ionospheric electrodynamic effects during sudden stratospheric warmings. *J. Geophys. Res.*, *115*, 1–9. doi: 10.1029/2010JA015273

Fenu, C., Reichel, L., & Rodriguez, G. (2016, 5). GCV for Tikhonov regularization via global Golub-Kahan decomposition. *Numerical Linear Algebra with Applications*, *23*(3), 467–484. Retrieved from `http://doi.wiley.com/10.1002/nla.2034` doi: 10.1002/nla.2034

Fritts, D. C., & Alexander, M. J. (2003). Gravity wave dynamics and effects in the middle atmosphere. *Reviews of Geophysics*, *41*(1). Retrieved from `https://agupubs.onlinelibrary.wiley.com/doi/abs/10.1029/2001RG000106` doi: 10.1029/2001RG000106

Goncharenko, L. P., Chau, J. L., Liu, H.-L., & Coster, A. J. (2010, 5). Unexpected connections between the stratosphere and ionosphere. *Geophys. Res. Lett.*, *37*(10), 1–6. doi: 10.1029/2010GL043125

Harding, B. J., Makela, J. J., Englert, C. R., Marr, K. D., Harlander, J. M., England, S. L., & Immel, T. J. (2017). The MIGHTI Wind Retrieval Algorithm: Description and Verification. *Space Science Reviews*, *212*, 585–600. doi: 10.1007/s11214-017-0359-3

Harding, B. J., Makela, J. J., & Meriwether, J. W. (2015). Estimation of mesoscale thermospheric wind structure using a network of interferometers. *Journal of Geophysical Research-Space Physics*, *120*, 3928–3940. doi: 10.1002/2015JA021025

He, M., & Chau, J. L. (2019). Mesospheric semidiurnal tides and near-12\,h waves through jointly analyzing observations of five specular meteor radars from three longitudinal sectors at boreal midlatitudes. *Atmospheric Chemistry and Physics*, *19*(9), 5993–6006. Retrieved from `https://www.atmos-chem-phys.net/19/5993/2019/` doi: 10.5194/acp-19-5993-2019

He, M., Chau, J. L., Stober, G., Li, G., Ning, B., & Hoffmann, P. (2018). Relations Between Semidiurnal Tidal Variants Through Diagnosing the Zonal Wavenumber Using a Phase Differencing Technique Based on Two Ground-Based Detectors. *Journal of Geophysical Research: Atmospheres*, *123*(8), 4015–4026. Retrieved from `https://agupubs.onlinelibrary.wiley.com/doi/abs/10.1002/2018JD028400` doi: 10.1002/2018JD028400

Hocking, W. K. (2005). A new approach to momentum flux determinations using SKiYMET meteor radars. *Annales Geophysicae*, *23*(7), 2433–2439. Retrieved from `https://www.ann-geophys.net/23/2433/2005/` doi: 10.5194/angeo-23 -2433-2005

Hocking, W. K. (2018, 6). Spatial distribution of errors associated with multistatic meteor radar. *Earth, Planets and Space*, *70*(1), 93. Retrieved from `https://doi.org/10.1186/s40623-018-0860-2` doi: 10.1186/s40623-018-0860-2

Hocking, W. K., Fuller, B., & Vandepeer, B. (2001, 1). Real-Time Determination of Meteor-Related Parameters Utilizing Modern Digital Technology. *Journal of Atmospheric and Solar-Terrestrial Physics*, *63*(2), 155–169.

Hoffmann, P., Singer, W., Keuer, D., Hocking, W. K., Kunze, M., & Murayama, Y. (2007). Latitudinal and longitudinal variability of mesospheric winds and temperatures during stratospheric warming events. *J. Atmos. Solar. Terr. Phys.*, *69*, 2355–2366.

Holdsworth, D. A. (2005). Angle of arrival estimation for all-sky interferometric meteor radar systems. *Radio Science*, *40*(RS6010). doi: 10.1029/2005RS003245

Holdsworth, D. A., Reid, I. M., & Cervera, M. A. (2004). Buckland {Park} all-sky interferometric meteor radar. *Radio˜Sci.*, *39*, doi:10.1029/2003RS003014.

Huyghebaert, D., Hussey, G., Vierinen, J., McWilliams, K., & St-Maurice, J. P. (2019, 4). ICEBEAR: An All-Digital Bistatic Coded Continuous-Wave Radar for Studies of the E Region of the Ionosphere. *Radio Science*, *54*(4), 349–364. doi: 10.1029/2018RS006747

Hysell, D. L., & Chau, J. L. (2002). Imaging Radar Observations and Nonlocal Theory of Large-Scale Waves in the Equatorial Electrojet. *Ann. Geophys.*, *20*, 1167–1179.

Hysell, D. L., Larsen, M. F., & Sulzer, M. P. (2014). High time and height resolution neutral wind profile measurements across the mesosphere/lower thermosphere region using the Arecibo incoherent scatter radar. *Journal of Geophysical Research-Space Physics*, *119*(3), 2345–2358. doi: 10.1002/(ISSN)2169-9402

Immel, T. J., England, S. L., Mende, S. B., Heelis, R. A., Englert, C. R., Edelstein, J., ... Sirk, M. M. (2018, 2). *The Ionospheric Connection Explorer Mission: Mission Goals and Design* (Vol. 214) (No. 1). Springer Netherlands. doi: 10.1007/s11214-017-0449-2

Immel, T. J., Sagawa, E., England, S. L., Henderson, S. B., Hagan, M. E., Mende, S. B., ... Paxton, L. J. (2006). The control of equatorial ionospheric morphology by atmospheric tides. *Geophys.˜Res.˜Lett.*, *33*(L15108). doi: 10.1029/2006GL026161

Jones, J., Webster, A. W., & Hocking, W. K. (1998). An improved interferometer design for use with meteor radars. *Radio˜Sci.*, *33*, 55–66.

Laskar, F. I., Chau, J. L., St.-Maurice, J. P., Stober, G., Hall, C. M., Tsutsumi, M., ... Hoffmann, P. (2017). Experimental Evidence of Arctic Summer Mesospheric Upwelling and Its Connection to Cold Summer Mesopause. *Geophysical Research Letters*, *44*(18), 9151–9158. Retrieved from `https://agupubs.onlinelibrary.wiley.com/doi/abs/10.1002/2017GL074759` doi: 10.1002/2017GL074759

Lee, K., Kudeki, E., Reyes, P. M., Lehmacher, G. A., & Milla, M. (2019, 12). Mesospheric Wind Estimation With the Jicamarca MST Radar Using Spectral Mainlobe Identification. *Radio Science*, *54*(12), 1222–1239. Retrieved from `https://onlinelibrary.wiley.com/doi/abs/10.1029/2019RS006892` doi: 10.1029/2019RS006892

Manson, A. H., Meek, C. E., Chshyolkova, T., Xu, X., Aso, T., Drummond, J. R., ... Ward, W. E. (2009). Arctic tidal characteristics at {Eureka} (80°{N}, 86°{W}) and {Svalbard} (78°{N}, 16°{E}) for 2006/07: seasonal and longitudinal variations, migrating and non-migrating tides. *Annales Geophysicae*, *27*(3), 1153–1173. doi:

10.5194/angeo-27-1153-2009

Meriwether, J., Faivre, M., Fesen, C., Sherwood, P., & Veliz, O. (2008). New results on equatorial thermospheric winds and the midnight temperature maximum. *Ann. Geophys*, *26*, 447–466.

Murphy, D. J., Forbes, J. M., Walterscheid, R. L., Hagan, M. E., Avery, S. K., Aso, T., ... Vincent, R. A. (2006, 12). A climatology of tides in the Antarctic mesosphere and lower thermosphere. *Journal of Geophysical Research: Atmospheres*, *111*(D23). Retrieved from http://doi.wiley.com/10.1029/2005JD006803 doi: 10.1029/2005JD006803

Nicolls, M. J., Cosgrove, R., & Bahcivan, H. (2014). Estimating the vector electric field using monostatic, multibeam incoherent scatter radarmeasurements. *Radio Science*. doi: 10.1002/2014RS005519

Oppenheim, M. M., Sugar, G., Slowey, N. O., Bass, E., Chau, J. L., & Close, S. (2009, 5). Remote sensing lower thermosphere wind profiles using non-specular meteor echoes. *Geophys. Res. Lett.*, *36*(9), 1–5. doi: 10.1029/2009GL037353

Pancheva, D., & Mukhtarov, P. (2011). Stratospheric warmings: The atmosphere-ionosphere coupling paradigm. *J.˜Atmos.˜Sol.˜Terr.˜Phys.*, *73*, in press. doi: 10.1016/j.jastp.2011.03.066

Pedatella, N. M., Chau, J. L., Schmidt, H., Goncharenko, L. P., Stolle, C., Hocke, K., ... Siddiqui, T. A. (2018). How sudden stratospheric warming affects the whole atmosphere. *Eos*, *99*. doi: 10.1029/2018EO092441

Pedatella, N. M., Liu, H.-L., Richmond, A. D., Maute, A., & Fang, T.-W. (2012, 8). Simulations of solar and lunar tidal variability in the mesosphere and lower thermosphere during sudden stratosphere warmings and their influence on the low-latitude ionosphere. *J. Geophys. Res.*, *117*(A08326). doi: 10.1029/2012JA017858

Rajaram, R., & Gurubaran, S. (1998). Seasonal variabilities of low-latitude mesospheric winds. *Annales Geophysicae*, *16*(2), 197–204. Retrieved from https://www.ann-geophys.net/16/197/1998/ doi: 10.1007/s00585-998-0197-4

Rao, S. V. B., Eswaraiah, S., Venkat Ratnam, M., Kosalendra, E., Kishore Kumar, K., Sathish Kumar, S., ... Gurubaran, S. (2014). Advanced meteor radar installed at Tirupati: System details and comparison with different radars. *Journal of Geophysical Research*, *119*, 11893–11904. doi: 10.1002/2014JD021781

Sandford, D. J., Muller, H. G., & Mitchell, N. J. (2006). Observations of lunar tides in the mesosphere and lower thermosphere at Arctic and middle latitudes. *Atmospheric Chemistry and Physics*, *6*(12), 4117–4127.

Shume, E. B., Hysell, D. L., & Chau, J. L. (2005). Zonal wind velocity profiles in the equatorial electrojet derived from phase velocities of type II radar echoes. *Journal of Geophysical Research*, *110*(A12), 8. Retrieved from papers2://publication/doi/10.1029/2005JA011210

Smith, A. K. (2012, 6). Global Dynamics of the MLT. *Surveys in Geophysics*, *33*(6), 1177–1230. doi: 10.1007/s10712-012-9196-9

Spargo, A. J., Reid, I. M., & MacKinnon, A. D. (2019, 9). Multistatic meteor radar observations of gravity-wave–tidal interaction over southern Australia. *Atmospheric Measurement Techniques*, *12*(9), 4791–4812. Retrieved from https://www.atmos-meas-tech.net/12/4791/2019/ doi: 10.5194/amt-12-4791-2019

Stober, G., & Chau, J. L. (2015). A multistatic and multifrequency novel approach for specular meteor radars to improve wind measurements in the {MLT} region. *Radio Science*, *50*(5), 431–442. Retrieved from http://dx.doi.org/10.1002/2014RS005591 doi: 10.1002/2014RS005591

Stober, G., Chau, J. L., Vierinen, J., Jacobi, C., & Wilhelm, S. (2018). Retrieving horizontally resolved wind fields using multi-static meteor radar observations. *Atmospheric Measurement Techniques Discussions*, *2018*, 1–25. Retrieved from https://www.atmos-meas-tech-discuss.net/amt-2018-93/ doi: 10.5194/amt-2018-93

Tsutsumi, M., Holdsworth, D. A., Nakamura, T., & Reid, I. M. (1999). Meteor observations with an MF radar. *Earth Planets Space*, *51*, 691–699.

Urco, J. M., Chau, J. L., Milla, M. A., Vierinen, J. P., & Weber, T. (2018). Coherent MIMO to Improve Aperture Synthesis Radar Imaging of Field-Aligned Irregularities: First Results at Jicamarca. *IEEE Transactions on Geoscience and Remote Sensing*, *PP*(99), 1–11. doi: 10.1109/TGRS.2017.2788425

Urco, J. M., Chau, J. L., Weber, T., Vierinen, J., & Volz, R. (2019). Sparse signal recovery in MIMO specular meteorradars with waveform diversity. *IEEE Trans. Geosci. Remote Sensing*, 1. Retrieved from `papers2://publication/uuid/3BE7DFC6-C58D-4567-AB89-92B77BC87721`

Vaudrin, C. V., Palo, S. E., & Chau, J. L. (2018). Complex Plane Specular Meteor Radar Interferometry. *Radio Science*, *53*(1), 112–128. Retrieved from `https://agupubs.onlinelibrary.wiley.com/doi/abs/10.1002/2017RS006317` doi: 10.1002/2017RS006317

Venkateswara Rao, N., Tsuda, T., & Kawatani, Y. (2012, 4). A remarkable correlation between short period gravity waves and semiannual oscillation of the zonal wind in the equatorial mesopause region. *Annales Geophysicae*, *30*(4), 703–710. Retrieved from `https://www.ann-geophys.net/30/703/2012/` doi: 10.5194/angeo-30-703-2012

Venkateswara Rao, N., Tsuda, T., Riggin, D. M., Gurubaran, S., Reid, I. M., & Vincent, R. A. (2012, 10). Long-term variability of mean winds in the mesosphere and lower thermosphere at low latitudes. *Journal of Geophysical Research: Space Physics*, *117*(A10), n/a-n/a. Retrieved from `http://doi.wiley.com/10.1029/2012JA017850` doi: 10.1029/2012JA017850

Vierinen, J., Chau, J. L., Charuvil, H., Urco, J. M., Clahsen, M., Avsarkisov, V., . . . Volz, R. (2019). Observing Mesospheric Turbulence With Specular Meteor Radars: A Novel Method for Estimating Second-Order Statistics of Wind Velocity. *Earth and Space Science*, *6*(7), 1171–1195. Retrieved from `https://agupubs.onlinelibrary.wiley.com/doi/abs/10.1029/2019EA000570` doi: 10.1029/2019EA000570

Vierinen, J., Chau, J. L., Pfeffer, N., Clahsen, M., & Stober, G. (2016). Coded continuous wave meteor radar. *Atmospheric Measurement Techniques*, *9*(2), 829–839. Retrieved from `https://www.atmos-meas-tech.net/9/829/2016/` doi: 10.5194/amt-9-829-2016

Vincent, R. A. (2015). The dynamics of the mesosphere and lower thermosphere: a brief review. *Progress in Earth and Planetary Science*, *2*(1), 4. Retrieved from `https://doi.org/10.1186/s40645-015-0035-8` doi: 10.1186/s40645-015-0035-8

Waldteufel, P., & Corbin, H. (1979). On the Analysis of Single-Doppler Radar Data. *J. Appl. Meteorol.*, *18*(2), 532–542. doi: 10.1175/1520-0450(1979)018⟨0532:OTAOSD⟩2.0.CO

Wallace, J. M., & Hobbs, P. V. (2006). *Atmospheric Science: An Introductory Survey: Second Edition*. doi: 10.1016/C2009-0-00034-8

Woodman, R. F., & Guillén, A. (1974). Radar observations of winds and turbulence in the stratosphere and mesosphere. *J. ̃Atmos. ̃Sci.*, *31*(2), 493–505.

Younger, J. P., & Reid, I. M. (2017). Interferometer angle-of-arrival determination using precalculated phases. *Radio Science*, *52*(9), 1058–1066. Retrieved from `https://agupubs.onlinelibrary.wiley.com/doi/abs/10.1002/2017RS006284` doi: 10.1002/2017RS006284

Receiver	Latitude (°)	Longitude (°)	Altitude (m)	Start Date	End Date
Ancon	-11.77	-77.15	72.00	20190902	running
Azpitia	-12.59	-76.62	69.92	20191004	running
Huancayo	-12.04	-75.32	3335.20	20190902	running
Sta Rosa	-11.66	-76.79	1160.75	20200227	running
Barranca	-10.80	-77.73	60.64	20190904	20200205
Huacho	-11.12	-77.61	58.10	20191004	20200205
La Cantuta	-11.96	-76.70	947.67	20200211	20200216
Mala	-12.66	-76.63	49.66	20190828	20191004
Obrajillo	-11.45	-76.62	2731.92	20200205	20200227
Oyon	-10.67	-76.77	3677.93	20191108	20200106

Table 1.   SIMONe Peru receiving stations used between September 2019 and April 2020.